

See discussions, stats, and author profiles for this publication at: <https://www.researchgate.net/publication/243374508>

Nitrous oxide decomposition on the binuclear $[\text{FeII}(\mu\text{-O})(\mu\text{-OH})\text{FeII}]$ Center in Fe-ZSM-5 zeolite

ARTICLE in THE JOURNAL OF PHYSICAL CHEMISTRY C · DECEMBER 2008

Impact Factor: 4.77 · DOI: 10.1021/jp808044r

CITATIONS

30

READS

19

3 AUTHORS, INCLUDING:



Guesmi Hazar

Pierre and Marie Curie University - Paris 6

36 PUBLICATIONS 235 CITATIONS

SEE PROFILE



Liubov Kiwi

École Polytechnique Fédérale de Lausanne

268 PUBLICATIONS 5,317 CITATIONS

SEE PROFILE

Article

**Nitrous Oxide Decomposition on the Binuclear
[Fe(μ -O)(μ -OH)Fe] Center in Fe-ZSM-5 Zeolite**

Hazar Guesmi, Dorothee Berthomieu, and Liubov Kiwi-Minsker

J. Phys. Chem. C, **2008**, 112 (51), 20319-20328 • DOI: 10.1021/jp808044r • Publication Date (Web): 04 December 2008

Downloaded from <http://pubs.acs.org> on February 12, 2009

More About This Article

Additional resources and features associated with this article are available within the HTML version:

- Supporting Information
- Access to high resolution figures
- Links to articles and content related to this article
- Copyright permission to reproduce figures and/or text from this article

[View the Full Text HTML](#)



ACS Publications
High quality. High impact.

The Journal of Physical Chemistry C is published by the American Chemical Society, 1155 Sixteenth Street N.W., Washington, DC 20036

Nitrous Oxide Decomposition on the Binuclear $[\text{Fe}^{\text{II}}(\mu\text{-O})(\mu\text{-OH})\text{Fe}^{\text{II}}]$ Center in Fe-ZSM-5 Zeolite

Hazar Guesmi,^{*,†} Dorothee Berthomieu,^{*,†} and Liubov Kiwi-Minsker[‡]

Ecole Nationale Supérieure de Chimie de Montpellier, Equipe MACS, Institut Charles Gerhardt, UMR 5253 CNRS/UM2/UM1, France, and Ecole polytechnique Fédérale de Lausanne, GGRC-ISIC, Station 6, CH-1015, Lausanne, Switzerland

Received: March 5, 2008; Revised Manuscript Received: November 3, 2008

The reaction mechanism for nitrous oxide (N_2O) direct decomposition into molecular nitrogen and oxygen was studied on binuclear iron sites in Fe-ZSM-5 zeolite using the density functional theory (DFT). Starting from the hydroxylated bi-iron complex $[\text{HOFe}^{\text{III}}(\mu\text{-O})(\mu\text{-OH})\text{Fe}^{\text{III}}\text{OH}]^+$, a reductive dehydroxylation pathway was proposed to justify the formation of the active site $[\text{Fe}^{\text{II}}(\mu\text{-O})(\mu\text{-OH})\text{Fe}^{\text{II}}]^+$. The latter contains two Fe^{II} ions linked via oxo and hydroxo bridges, $\text{Z}^-[\text{Fe}^{\text{II}}(\mu\text{-O})(\mu\text{-OH})\text{Fe}^{\text{II}}]^+$, and for the first time was considered to catalyze the N_2O decomposition. The DFT results show the activity of $[\text{Fe}^{\text{II}}(\mu\text{-O})(\mu\text{-OH})\text{Fe}^{\text{II}}]^+$ complex for the N_2O decomposition. The first step of the catalytic reaction corresponds to a spontaneous adsorption of N_2O over Fe^{II} sites, followed by the surface atomic oxygen loading and the release of molecular nitrogen. The formation of molecular O_2 occurs through the migration of the atomic oxygen from one iron site to another one followed by the recombination of two oxygen atoms and the desorption of molecular oxygen. The computed reactivity over the binuclear iron core complex $[\text{Fe}^{\text{II}}(\mu\text{-O})(\mu\text{-OH})\text{Fe}^{\text{II}}]^+$ is consistent with experimental data reported in the literature. Although the dissociation steps of the N_2O molecules, calculated with respect to adsorbed N_2O intermediates, are highly energetic, the energy barrier associated with the atomic oxygen migration is the highest one. Up to 700 K, the oxygen migration step has the highest free energy barrier, suggesting that it is the rate-limiting step of the overall kinetics. This result explains the absence of O_2 formation in experimental study of N_2O decomposition at temperatures below 623 K.

1. Introduction

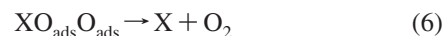
Industrial processes of gaseous effluent cleanup from mobile sources and industrial waste streams are of particular importance for environmental protection. Transition metal ion-exchanged in a zeolite matrix is an efficient catalyst in NO_x abatement. Example of such catalysts are Cu-ZSM-5 and Fe-ZSM-5, which decompose N_2O into N_2 and O_2 .¹ From an experimental viewpoint, while the activation energy of the N_2O noncatalytic decomposition is 60–65 kcal/mol,² in the presence of Fe-ZSM-5 catalyst this energy decreases to around 28–45 kcal/mol.^{3–7} The mechanism of the reaction catalyzed by transition metals in zeolites is still under debate. A lot of studies have been recently devoted to Fe-ZSM-5, which is considered as a model catalyst that helps understands catalytic reactions by these materials.⁸ Fe-ZSM-5 was shown to be very efficient not only in the N_2O decomposition but also in the oxidation of alkenes and aromatics using N_2O as oxidant.^{9,10} According to several authors, it has been concluded that the common feature of these two reactions catalyzed by Fe-ZSM-5 is the formation of adsorbed oxygen atoms called “ α -oxygen” or “ O_{ads} ” (eq 1).



Although extensive experimental and theoretical studies have been devoted to the understanding of the mechanism of the N_2O decomposition, the nature, the nuclearity, and valence of the active iron sites^{3–7,11,12} as well as the rate-limiting step^{13–17}

are still debated. However, it is generally admitted that whatever the preparation methods, several types of iron are present in Fe-ZSM-5.¹⁸

Theoretical approaches have reported two alternative models containing extra-framework iron sites.^{15,17,19–23} The first one proposed by Yoshizawa et al.²¹ and subsequently developed by Ryder et al.²² and Heyden et al.^{17,24} consists of an isolated iron site with various valence states. Consistent with this model, it has been concluded that isolated iron cations bound to a single oxygen atom $\text{Z}^-[\text{FeO}]^+$ (Z^- represents the zeolite) are active. In contrast, it has been concluded that $\text{Z}^-[\text{Fe}]^+$ is not active.^{21,22} Moreover, the $\text{Z}^-[\text{FeO}]^+$ species leads to the formation of two active intermediates $\text{Z}^-[\text{FeO}_2]^+$ and $\text{Z}^-[\text{OFeO}]^+$, which are catalytically active for the decomposition of a second N_2O molecule, resulting in O_2 formation (see eqs 2–6).



The second investigated model involves binuclear iron sites. The formation and high activity of oxygen-bridged binuclear species were suggested by numerous experimental studies,^{25–29} but only few theoretical approaches have been reported in the literature. Investigations of binuclear iron sites in the ZSM-5 extra-framework position have considered the reactivity of a

* Corresponding authors. E-mails: hazar.guesmi@enscm.fr, berthomieu@univ-montp2.fr.

[†] Ecole Nationale Supérieure de Chimie de Montpellier.

[‡] Ecole polytechnique Fédérale de Lausanne.

[Fe–O–Fe]²⁺ binuclear species as well as the hydrated [HOFe–O–FeOH]²⁺ in which the iron valencies are Fe^{II} and Fe^{III}, respectively.^{17,23,30,31} As for isolated iron sites, it has been concluded that only dehydrated species are active for N₂O decomposition. It has been reported also that the N₂O dissociation is the rate-limiting step controlling the overall reaction kinetics. The activation energy of the latter process was found to be of the same order of magnitude for binuclear [FeOFe]²⁺ (21.0 kcal/mol)³⁰ and for isolated [FeO]⁺ (24.3 kcal/mol).¹⁷

In contrast with these theoretical results, Kiwi-Minsker and co-workers⁵ have reported a different N₂O kinetic behavior “suggesting that the high activity of HZSM-5 with a high Si/Al ratio and low iron content could be explained by the presence of binuclear iron sites”.^{32,33} From a quantitative study³² enriched by results from the literature, these authors proposed a tentative structure made of an active binuclear Fe center featuring a diamond core geometry [Fe₂O₂H]⁺, similar to that of monooxygenase (MMO) enzyme. In addition, from transient and steady-state kinetics⁵ studied over Fe-ZSM-5 catalysts they concluded that (i) the N₂O reaction involves reversible adsorption of N₂O, (ii) interaction of adsorbed N₂O with a vacant Fe-site leads to the formation of N₂ and (O_{ads}), and (iii) molecular oxygen formation occurs by recombination of two (O_{ads}). The authors claim that the slow O₂ formation/desorption is the rate-limiting step in the overall catalytic reaction. These interpretations are also consistent with other numerous experimental reports.^{4,13,34,35}

A binuclear active Fe-center in Fe-ZSM-5, with a structure similar to that of MMO enzyme, has been mentioned for the first time by Panov and co-workers.³⁶ These authors observed that Fe/MFI catalysts with low Fe loading that were treated at a high temperature are able to abstract an oxygen atom from an impinging N₂O molecule at 523 K, without releasing O₂ into the gas phase. This special form of adsorbed α -oxygen³⁷ was shown to have remarkably high reactivity similar to the active oxygen of enzyme monooxygenase.³⁸ Using EXAFS techniques, Prins and co-workers²⁵ have determined the geometrical parameters of binuclear Fe-center in Fe-ZSM-5 zeolites and have also assigned iron complex geometry to the MMO type. Unlike the binuclear oxygen-bridged Fe^{II} sites, [FeOFe]²⁺, recently calculated,^{23,30} the present binuclear Fe-center includes both oxo- and hydroxo- bridges and therefore has an overall monopositive charge suitable to compensate for the negative charge of the zeolite lattice introduced by a single Al atom in the vicinity. One of the reasons for the interest in such a cluster is that the presence of only one Al instead of two Al atoms in the lattice increases the probability that a [Fe₂O₂H]⁺ structure exists in zeolites with high Si/Al ratios.^{39,40} Indeed, using the statistical method, Race and co-workers⁴⁰ reported that the probability of Al pairs occurring in the high-silica zeolites is very small.

According to numerous experimental studies on the nature of iron sites in Fe-ZSM-5 regarding the zeolite preparation/activation steps,^{25,29,41} it has been concluded that iron first exists as isolated Fe species with tetrahedral coordination, which upon subsequent steaming and calcination are transformed into hydroxylated binuclear complexes.^{25,33} In this structure, iron cations are in the oxidation state Fe^{III} and are completely inactive for the N₂O decomposition.^{30–33} As shown by DRIFT experiments,^{25,32} calcination at high temperature in an inert atmosphere (He flow) leads to dehydroxylation and concomitant autoreduction of the binuclear Fe^{III} complex which generates the active Fe^{II} species.

In the present paper, we first consider possible hydroxylated iron site structures which were revealed by EXAFS experiments.²⁵ Additionally we report a possible pathway for the

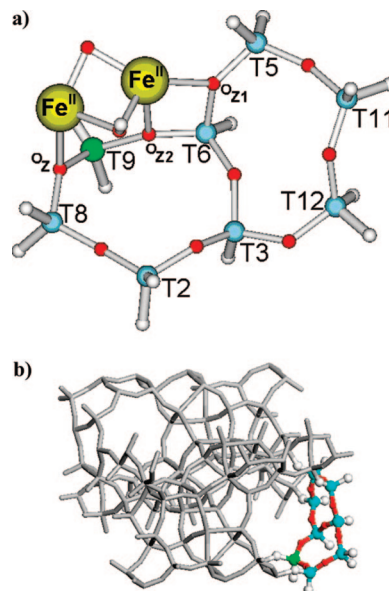


Figure 1. (a) The di-iron center ([Fe(μ -O)(μ -OH)Fe]⁺) inserted in part of the zeolite framework. Small gray balls are H, large gray balls are Fe, blue balls are Si, green ball is Al, and red balls are O. (b) Localization of (Z[−]) cluster inside ZSM-5 zeolite.

dehydroxylation and autoreduction process resulting in the (μ -oxo)(μ -hydroxo)-bridged binuclear iron complex. According to experiments, this latter mechanism would take place at high temperature during steaming and activation procedures^{14,32,33} which leads to the release of water molecules. Then we report mechanistic and energetic aspects of the N₂O decomposition into N₂ and O₂ over the binuclear [Fe^{II}(μ -O)(μ -OH)Fe]⁺ site. We consider and analyze an O delivery system, inspired by previous theoretical studies,^{23,30} to reveal the complete energy profile of N₂ and O₂ formation in the Fe-ZSM-5 catalytic cycle and to compare to experimental results. We also analyze the influence of antiferromagnetic coupling of the two iron centers on the reaction mechanism of the N₂O decomposition. Finally, in the last section of the paper, we discuss how our computed electronic and free energies allow a better understanding of experimental data published in the literature.

2. Computational Details

The modeled active site was composed by a positive di-iron center [Fe(μ -O)(μ -OH)Fe]⁺ inserted in part of the zeolite framework Z[−] (Figure 1a). The cluster model Z consists of two 5T (tetrahedra are labeled T) rings (also noted M5; the M notation stands for sites located in the main channel and 5 for 5-fold rings) shearing an edge representing part of the wall of the straight channel of the ZSM-5 structure (Figure 1b). The Z[−] cluster,¹⁷ the dangling bonds of which were saturated by H atoms, is similar to the one used by Hensen et al.³⁰ and A. L. Yakovlev et al.²³ The only difference is the existence of only one Al atom substituting preferentially the Si of T9 position.⁴² (Figure 1a).

Quantum chemical calculations and transition state structures on potential energy surfaces (PES) and minimum energy structures on the seam of two PES were performed using nonlocal, gradient-corrected density functional theory (DFT).⁴³ The B3LYP hybrid functional^{44,45} was used since it has been shown to give accurate results in the literature.^{17,23,30} Basis sets at the triple- ξ level with polarization functions TZVP⁴⁶ were used for all atoms including iron [H (311/1); O (62111/411/1); Fe (842111/631/411/1); Al and Si (73211/6111/1)]. No correc-

tions were made for basis set superposition error (BSSE).⁴⁷ Calculations and reported values were carried out using the Gaussian 03 package.⁴⁸

Geometries were optimized with an energy convergence criterion of at least 10^{-7} Ha and a maximum norm of the Cartesian gradient of 10^{-4} Ha/Bohr. TS (first-order saddle point) were localized using the Synchronous Transit-Guides Quasi-Newton (STQN)⁴⁹ method as implemented in Gaussian 03. A gradient norm convergence criterion of 4×10^{-4} Ha/Bohr was reached. Frequency calculations were done in order to check that the stationary points, minima and TS, exhibit the proper number of imaginary frequencies: none for a minimum and one for a transition state. Thereby, to account correctly for the fixed atoms additional frequency calculations were performed in which the components of the fixed atoms are carved out of the Cartesian second derivative matrix.⁵⁰ Reported frequency values were calculated taking into account all the atoms with respect to the structure. All calculations and reported values were zero point corrected.

PES minima were calculated for all spin surfaces (i.e., spin multiplicity $M_s = 1-11$). Analysis of these different spin surfaces reveals that only the energies of high-spin (HS) states (nonet PES corresponding to $M_s = 9$ and/or 11-et PES corresponding to $M_s = 11$) needed to be considered since they are the most stable spin states. Therefore, only HS minimum energy PESs are reported in this paper.

In reactions involving change in the spin state, the stationary points governing chemical reactivity lie on different PESs. These reactions have attracted much attention, particularly in the branch of organometallic chemistry.⁵¹ It is assumed that a spin transition, which differs from a transition state, occurs in the region where two spin surfaces cross. The algorithm required to locate the Minimum Energy Crossing Point (MECP) involves an energy minimization on one surface under the constraint that two surfaces have the same energy. All that is needed is to be able to compute the energy and gradient on both surfaces, which can easily be done with available programs. The particular implementation developed by Harvey and co-workers^{52,53} and used in this work in conjunction with Gaussian03 packages has already been used to locate MECP on systems involving transition metal atoms.^{52,54} The converged minimum energy crossing point structure corresponds to the maximum energy difference between both PESs of 5×10^{-6} Ha.

In order to evaluate the effect of antiferromagnetic coupling between the two iron centers on the mechanistic aspects of N_2O catalytic cycle, broken symmetry-based calculations for a set of reactions were considered. These calculations were applied to the adsorption and dissociation of N_2O molecule steps and compared to the high-spin states. The spin coupling parameter J was calculated using the nonprojected approach (eq 7) which was demonstrated to give accurate coupling constants.⁵⁵

$$E_{HS} - E_{BS} = -(2S_1S_2 + S_2)J \quad (7)$$

E_{HS} corresponds to the high-spin solution and E_{BS} corresponds to the broken-symmetry solution where opposite spins at the two paramagnetic centers are achieved by DFT calculations. S_1 and S_2 are total spins of the two paramagnetic centers.

For free energy calculations ($G = H - TS$), thermodynamic properties were computed using standard statistical mechanics within the harmonic approximation. Entropic values include the contributions of the transitional, rotational, vibrational, and electronic partition function for zeolite cluster and for all gaseous species involved in the reaction.⁵⁶

TABLE 1: Relative Energies, Calculated at the B3LYP/TZVP Level of Theory, of Optimized Hydroxylated $Z-[Fe_2O_4H_3]^+$ Structures^a

configuration	energy (kcal/mol)
A	0.0
B	7.9
C	11.0
D	38.9
E	40.9

^a The reported values were carried using a special Z^- cluster comprising H-terminations for silicon atoms and extended terminations, O-Si-H₃, for an Al atom.

TABLE 2: Comparison between Optimized Structure A of Hydroxylated (μ -Oxo)(μ -hydroxo)-Bridged Binuclear Iron Complex and EXAFS Measurements Reported in the Literature^a

	Fe-Fe, Å	Fe-(μ -O), Å	Fe-(μ -OH), Å	ref
[HOFe ^{III} (μ -O)(μ -OH)Fe ^{III} OH] ⁺	2.80	1.84	2.01	this work
EXAFS analysis in MMOH	2.83	1.85	1.98	60
EXAFS analysis in MMOH	2.91	1.82	1.99	61
EXAFS analysis in Fe-ZSM-5	3.05	1.83	1.94	25
EXAFS analysis in Fe-ZSM-5	3.07	1.85	1.97	26

^a The EXAFS geometric parameters of binuclear core structure are extracted from references 60 and 61 for MMOH and from 25 and 26 for octahedral di-iron complexes in Fe-ZSM-5.

3. Results and Discussion

3.1. Z^- [HOFe(μ -O)(μ -OH)FeOH]⁺ Complex. 3.1.1. Structure Parameters. Applied after the hydrolysis steps, several spectroscopic techniques^{25,26,38} on Fe-ZSM-5 samples have revealed a binuclear iron structure different from those postulated in the literature^{29,57,58} and similar to the so-called “diamond core” structure of the active site in the MMO enzyme.⁵⁹ Prins and co-workers²⁵ have proposed various shell models consisting of different back scattering pairs fitting the EXAFS spectrum of iron sites in ZSM-5 zeolite. One of the corresponding models presented as [HOFe^{III}(μ -O)(μ -OH)Fe^{III}OH]⁺ is considered in the present work. To the best of our knowledge, diamond structure included in a ZSM-5 zeolite cluster framework has never been modeled. It is then of prime importance to check if such structure configuration (oxo and hydroxo bridged on binuclear iron site) is favorable inside a ZSM-5 zeolite and if the structure parameters are consistent with experimental findings. As shown in Table 1, a series of five possible hydrated Fe^{III} structures have been compared: (A) Z^- [HOFe^{III}(μ -O)(μ -OH)Fe^{III}OH]⁺; (B) Z^- [(HO)₂Fe^{III}(μ -O)Fe^{III}OH]⁺; (C) Z^- [HOFe^{III}(μ -O)Fe^{III}(OH)₂]⁺; (D) Z^- [HO-O-Fe^{III}(μ -OH)Fe^{III}OH]⁺; (E) Z^- [HOFe^{III}(μ -OH)Fe^{III}O-OH]⁺. The optimized structures show that the most stable configuration corresponds to configuration A; i.e., the complex containing both oxo and hydroxo bridges. We can also check, from Table 2, the high concordance of structure parameters with experimental findings. The optimized [HOFe(μ -O)(μ -OH)-FeOH]⁺ (A) structure parameters (Table 2) are in good agreement with EXAFS data for the hydroxylated models of the iron site in Fe-ZSM-5 obtained by Prins et al.²⁵ and Battiston et al.²⁶ One can also find EXAFS results on the structure of the active center of methane monooxygenase enzyme^{60,61} which confirms the high similarity of the optimized binuclear structure with the binuclear core structure in MMOH.

3.1.2. Activation Processes of Binuclear Iron Sites. According to experimental data, the formation of the Fe^{II} iron active sites would be the result of high temperature ($T > 1000$ K) reductive dehydroxylation of the binuclear Fe^{III} complex giving

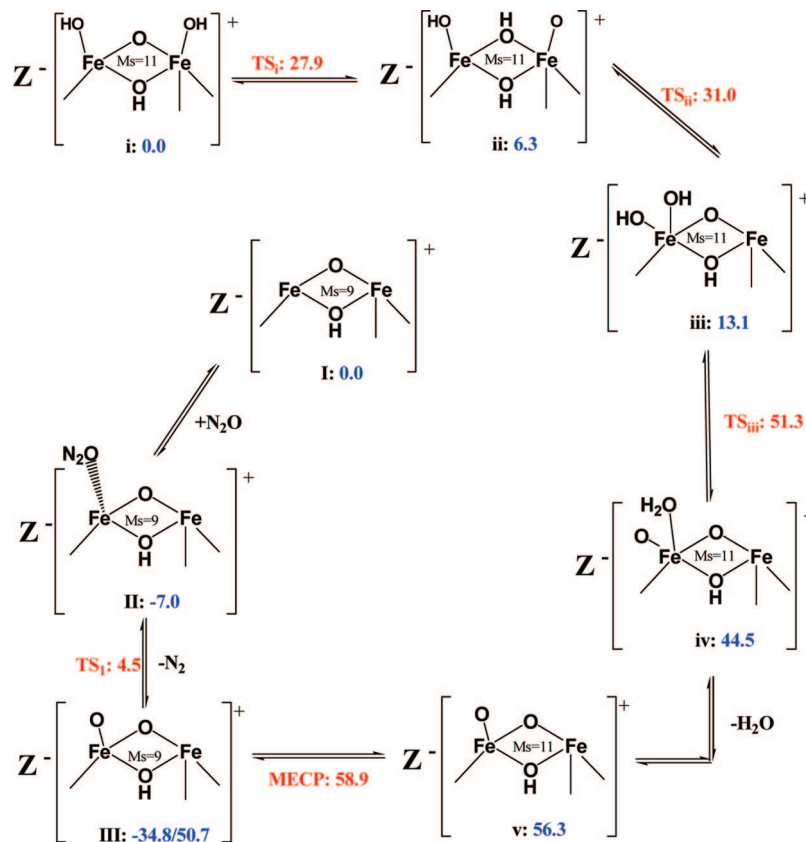


Figure 2. Calculated path of reductive hydroxylation process resulting in the binuclear active site (structure I). Reported energies are in kcal/mol and are zero-point corrected. Energies are calculated with reference to configuration i with appropriate amounts of H₂O and with reference to configuration I with appropriate amount of N₂O and N₂. Energies of potential energy minima are presented in blue color. Energies of transition states and energies of minima on the seam of two PESs (MECP) are presented in red color.

the key structure of the active site for N_2O decomposition. Our DFT calculations suggest a possible minimum energy pathway for the dehydration and autoreduction processes which is reported in Figure 2. The dehydration reaction (from structure **i** to structure **v**) consists of a sequence of four highly endothermic elementary reactions leading to a binuclear iron intermediate with adsorbed oxygen. The highest reaction barrier of the latter process is equal to 38.2 kcal/mol. As a result, the overall barrier for the dehydration reaction $\text{Z}^-[\text{HO-Fe}^{\text{III}}(\mu\text{-O})(\mu\text{-OH})\text{Fe}^{\text{III}}\text{-OH}]^+ (\textbf{i}) \rightarrow \text{Z}^-[\text{Fe}^{\text{III}}(\mu\text{-O})(\mu\text{-OH})\text{Fe}^{\text{III}}\text{-O}]^+ (\textbf{v}) + \text{H}_2\text{O}$, which is calculated as the energy difference between $\text{Z}^-[\text{Fe}^{\text{III}}(\mu\text{-O})(\mu\text{-OH})\text{Fe}^{\text{III}}\text{-O}]^+ (\text{Ms} = 11) + \text{H}_2\text{O}$ and $\text{Z}^-[\text{HO-Fe}^{\text{III}}(\mu\text{-O})(\mu\text{-OH})\text{Fe}^{\text{III}}\text{-OH}]^+ (\text{Ms} = 11)$, is 56.3 kcal/mol. The $\text{Z}^-[\text{Fe}(\mu\text{-O})(\mu\text{-OH})\text{Fe-O}]^+$ structure is more stable on the nonet PES (50.7 kcal/mol for structure **III**) than on the 11-et PES (56.3 kcal/mol for structure **v**). A small spin change barrier of 2.6 kcal/mol was found for the spin inversion process. At this step the autoreduction of the binuclear iron site occurs. The iron cations are already in the oxidation state +2 and adsorbed oxygen being in its singlet states can react with nitrogen molecule to give intermediate **II**. From the latter, bound nitrous oxide molecules can be easily released. As a result, the active $(\mu\text{-oxo})(\mu\text{-hydroxo})$ -bridged binuclear iron site (configuration **I**) is generated. The overall process of dehydroxylation and autoreduction of $[\text{HOFe}^{\text{III}}(\mu\text{-O})(\mu\text{-OH})\text{Fe}^{\text{III}}\text{OH}]^+$ precursor is strongly endothermic and explains the experimental high temperature treatments needed for the zeolite activation.^{5,32,33}

3.2. Catalytic Cycle of N₂O Decomposition over Z[−][Fe(μ -O)(μ -OH)Fe]⁺ Complex. In the following, we report and discuss PES investigated at 0 K for the N₂O decomposition over the (μ -oxo)(μ -hydroxo) binuclear iron complex, Z[−][Fe^I(μ -O)(μ -

OH)Fe²⁺]⁺. The two Fe^I and Fe^{II} iron cations are in oxidation state +2 and are coordinated to one and two framework oxygen atoms, respectively. The reaction pathway of the catalytic cycle of N₂O decomposition reported in Figure 3 occurs through N₂O adsorption and N₂ dissociation steps (from configuration **I** to configuration **V**) followed by the atomic oxygen migration and O₂ recombination–desorption processes (from configuration **VI** to configuration **VIII**). Distances to the nearest neighbors in the first coordination sphere of the iron cations in configurations and intermediates described below are presented in Table 3.

3.2.1. Minimum Energy Reaction Path. As shown in Figure 3, we investigated two possible reaction pathways for N_2O decomposition on dehydroxylated binuclear site $\text{Z}^-[\text{Fe}^{\text{I}}(\mu\text{-O})(\mu\text{-OH})\text{Fe}^{\text{II}}]^+$ (**I**). We discuss herein the reaction profile from $\text{Z}^-[\text{Fe}^{\text{I}}(\mu\text{-O})(\mu\text{-OH})\text{Fe}^{\text{II}}]^+$ (**I**) to $\text{Z}^-[\text{O}_2\text{-Fe}^{\text{I}}(\mu\text{-O})(\mu\text{-OH})\text{Fe}^{\text{II}}]^+$ (**VIII**) via $\text{Z}^-[\text{OFe}^{\text{I}}(\mu\text{-O})(\mu\text{-OH})\text{Fe}^{\text{II}}]^+$ (**III**). The reaction profile via $\text{Z}^-[\text{Fe}^{\text{I}}(\mu\text{-O})(\mu\text{-OH})\text{Fe}^{\text{II}}\text{O}]^+\text{Z}^-$ (**IIIa**) is very similar, with a slight preference for the N_2O molecule to adsorb over less-coordinated iron atom Fe^{I} ($\Delta E = 0.6$ kcal/mol). The nitrogen oxide molecule is adsorbed by its O-end with a relatively large bond length ($d_{\text{Fe-O}} = 2.35$ Å). The adsorption enthalpy is $\Delta H_{\text{ads}} = -7.1$ kcal/mol (Table 4). This value is smaller than experimental values reported by several authors (Wood et al., -15 kcal/mol;⁶² Kiwi-Minsker et al., -12.7 kcal/mol⁵) but higher than the one calculated by Hansen et al.³⁰ for nitrous oxide adsorption over binuclear cluster $\text{Z}^{2-}[\text{FeOFe}]^{2+}$ ($\Delta H_{\text{ads}} = -2.7$ kcal/mol). To eliminate the dinitrogen molecule, the reaction occurs through the TS_1 transition state. The activation barrier for the reaction of $\text{Z}^-[(\text{N}_2\text{O})\text{Fe}^{\text{I}}(\mu\text{-O})(\mu\text{-OH})\text{Fe}^{\text{II}}]^+$ (**II**) to form $\text{Z}^-[\text{OFe}^{\text{I}}(\mu\text{-O})(\mu\text{-OH})\text{Fe}^{\text{II}}]^+$ (**III**) and N_2 is $E^\ddagger = 11.5$ kcal/mol. The enthalpy of the reaction of $\text{Z}^-[(\text{N}_2\text{O})\text{Fe}^{\text{I}}(\mu\text{-O})(\mu\text{-OH})\text{Fe}^{\text{II}}]^+$ (**II**) to form $\text{Z}^-[\text{OFe}^{\text{I}}(\mu\text{-O})(\mu\text{-OH})\text{Fe}^{\text{II}}]^+$ (**III**) and N_2 is $E^\ddagger = 11.5$ kcal/mol. The enthalpy of the reaction of $\text{Z}^-[(\text{N}_2\text{O})\text{Fe}^{\text{I}}(\mu\text{-O})(\mu\text{-OH})\text{Fe}^{\text{II}}]^+$ (**II**) to form $\text{Z}^-[\text{OFe}^{\text{I}}(\mu\text{-O})(\mu\text{-OH})\text{Fe}^{\text{II}}]^+$ (**III**) and N_2 is $E^\ddagger = 11.5$ kcal/mol.

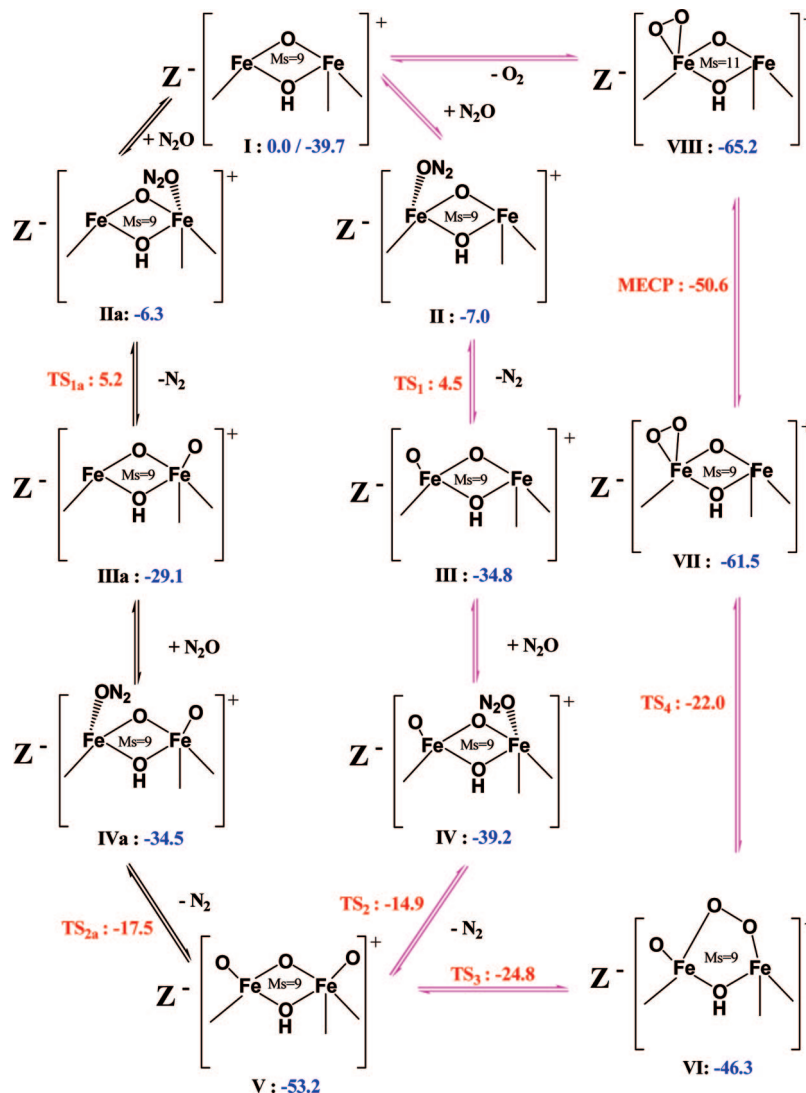


Figure 3. Calculated paths of N₂O decomposition with energies in kcal/mol. Energies are zero-point corrected and calculated with reference to configuration I with appropriate amounts of N₂O, N₂, and O₂. Energies of potential energy minima are presented in blue color. Energies of transition states and MECP are presented in red color.

TABLE 3: Distances (Å) to the Nearest Neighbors in the First Coordination Sphere of the Iron Cations^a

configuration	Fe–Fe	Fe ¹					Fe ²					
		μ–O	μ–OH	O _z	O ₍₁₎	O _{NN}	μ–O	μ–OH	O _{z1}	O _{z2}	O ₍₂₎	O _{NN}
I	2.48	1.84	2.14	2.03	—	—	1.84	2.01	2.3	2.15	—	—
II	2.53	1.86	2.13	2.05	—	2.35	1.84	2.01	2.28	2.17	—	—
III	2.63	1.76	2.07	2.08	1.63	—	1.88	1.99	2.16	2.16	—	—
IV	2.64	1.77	2.05	2.07	1.63	—	1.9	2.01	2.19	2.17	—	2.53
V	2.74	1.78	2.04	2.02	1.63	—	1.83	2.03	2.20	2.12	1.62	—
VI	2.81	1.81 ^b	2.10	2.13	1.63	—	1.89 ^b	1.94	2.16	2.17	—	—
VII	2.62	1.81	2.04	2.08	2.03	—	1.87	2.01	2.17	2.16	—	—
VIII	2.61	1.82	2.05	2.08	2.04	—	1.87	2.01	2.18	2.17	—	—

^a Distances shorter than 2.5 Å are shown only. Reported configurations correspond to the computed local minima of the N₂O decomposition path illustrated in Figure 3. Fe¹ and Fe² iron cations are coordinated to one (O_z) and two (O_{z1}, O_{z2}) framework oxygen atoms, respectively. O_{NN}, O₍₁₎ and O₍₂₎ correspond to the adsorbed nitrous oxide O-end, first and second formed oxo-species, respectively. ^b Bond length of first neighboring iron–oxygen; O–O bond length in the μ-peroxo equals 1.41 Å.

OH)Fe²⁺ (II) into Z[−][OFe¹(μ-O)(μ-OH)Fe²⁺] (III) + N₂ is very exothermic with ΔH_R = −27.1 kcal/mol.

The second N₂O dissociation occurs through a similar process. Z[−][OFe¹(μ-O)(μ-OH)Fe²⁺] (III) is in turn an active site for the decomposition of a N₂O molecule. The latter is adsorbed by its O-end on the unoccupied iron atom (Fe²) with ΔH_{ads} = −4.6

kcal/mol. The activation energy value E^{\ddagger} of the reaction of Z[−][OFe¹(μ-O)(μ-OH)Fe²⁺](ON₂) (IV) into Z[−][OFe¹(μ-O)(μ-OH)Fe²⁺] (V) + N₂ is 24.3 kcal/mol. On binuclear oxygen-bridged iron sites Hansen et al.³⁰ calculated, at the same level of theory, higher energy barriers for the dissociation of N₂O. Activation energies E^{\ddagger} of 25.6 and 30.1 kcal/mol have been

TABLE 4: Energetic Parameters of All Elementary Steps Computed for the N₂O Decomposition Path^a

elementary step	ΔH_{ads} (kcal/mol)	activation energy barrier (kcal/mol)	ΔH_{R} (kcal/mol)
I → II	−7.1	—	—
II → TS ₁	—	11.5	—
II → III + N ₂	—	—	−27.1
III → IV	−4.6	—	—
IV → TS ₂	—	24.3	—
IV → V + N ₂	—	—	−13.5
V → TS ₃ → VI	—	28.4	6.6
VI → TS ₄ → VII	—	24.3	−14.4
VII → MECP → VIII	—	10.8	−3.7
VIII → I + O ₂	25.8	—	—

^a Reported activation energy barriers are calculated as the difference between the energy of the TS state and the energy of the reactant. Minimum Energy Crossing Point (MECP) corresponds to the intersection of the two spin surfaces of configurations **VII** and **VIII**.

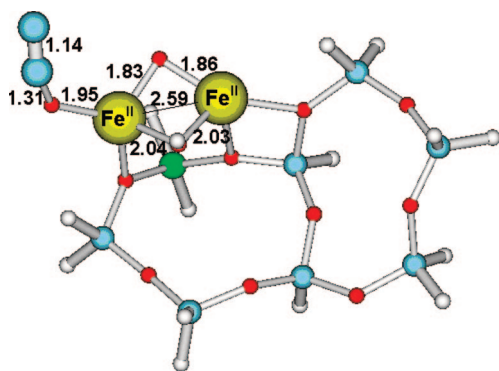


Figure 4. TS₁ localized transition structure. Small gray balls are H, large gray balls are Fe, blue balls are Si, green ball is Al, red balls are O, and large blue balls are N. Bond length values are indicated in angstroms.

reported for the N₂ elimination after the adsorption of the first and second N₂O molecules, respectively. In our computed reaction pathway, N₂ elimination process (**IV** ↔ **V**) is found to be exothermic with an enthalpy of reaction $\Delta H_{\text{R}} = -13.5$ kcal/mol. With respect to the N₂O and N₂ gas phase molecules, the intermediate $Z^-[\text{OFe}^1(\mu\text{-O})(\mu\text{-OH})\text{Fe}^2\text{O}]^+$ (**V**) is highly stable in comparison to **I**, ($\Delta E = -53.2$ kcal/mol). At this stage of the catalytic reaction a complete coverage of active Fe sites by oxo-species is expected to be achieved. The adsorption of a third N₂O molecule over one of the two iron cations already saturated by an oxygen atom is calculated to be endothermic ($\Delta H_{\text{ads}} = 16.7$ kcal/mol). Therefore, the dissociation of two N₂O molecules over only one iron atom is very unlikely to occur.

Molecular oxygen formation proceeds via the migration of an oxygen atom from one iron atom to the other one. The oxygen atom bound to the Fe² atom migrates across the μ -oxo bridge. During this process a stable minimum **VI**, drawn as a (μ -peroxo)(μ -hydroxo)-bridging binuclear iron core, was located. The enthalpy of the rearrangement of $Z^-[\text{OFe}^1(\mu\text{-O})(\mu\text{-OH})\text{Fe}^2\text{O}]^+$ (**V**) into $Z^-[\text{OFe}^1(\mu\text{-O-O})(\mu\text{-OH})\text{Fe}^2]^+$ (**VI**) is slightly endothermic with $\Delta H_{\text{R}} = 6.6$ kcal/mol (Table 4). To achieve this first migration step, a high activation energy of $E^\ddagger = 28.4$ kcal/mol is needed. Intermediate **VI** reacts to give a superoxide structure $Z^-[\text{O}_2\text{Fe}^1(\mu\text{-O})(\mu\text{-OH})\text{Fe}^2]^+$ (**VII**) in which molecular oxygen is preformed. This latter reaction is exothermic with an enthalpy of reaction $\Delta H_{\text{R}} = -14.4$ kcal/mol. The activation energy of the reaction from $Z^-[\text{OFe}^1(\mu\text{-O-O})(\mu\text{-OH})\text{Fe}^2]^+$ (**VI**) to form $Z^-[\text{O}_2\text{Fe}^1(\mu\text{-O})(\mu\text{-OH})\text{Fe}^2]^+$ (**VII**) is 24.4 kcal/mol. The

latter structure is stable on the nonet PES and corresponds to adsorbed molecular oxygen, in its singlet state, over one of the two iron cations. Molecular oxygen desorption in its ground triplet state requires a spin surface crossing from the nonet (**VII**) to the 11-et (**VIII**) PES structures. The spin inversion process occurs without significant geometry variation and a small exothermic enthalpy of reaction $\Delta H_{\text{R}} = -3.7$ kcal/mol. A small spin change barrier of $E^\ddagger = 10.8$ kcal/mol is needed to get the superoxide structure on the 11-et PES. As a last step of the catalytic cycle, a high endothermic molecular desorption process occurs. O₂ desorbs from $Z^-[\text{O}_2\text{Fe}^1(\mu\text{-O})(\mu\text{-OH})\text{Fe}^2]^+$ in the 11-PES with an enthalpy of desorption of $\Delta H_{\text{des}} = 25.8$ kcal/mol.

3.2.2. Natural Population Analysis and Frequency Calculations.

Analysis of natural population variations in the spin and charge densities have been performed in order to get some insight on the iron valences. As reported in Table 5, the iron cations of the active site $Z^-[\text{Fe}^1(\mu\text{-O})(\mu\text{-OH})\text{Fe}^2]^+$ are Fe^{II}–Fe^{II} species, with approximately a spin population of 4 on each Fe-center (3.60 for Fe^I and 3.62 for Fe²). N₂O adsorbs over the less coordinated iron site with a large Fe–O bond length (configuration **II**); thereby, the adsorption occurs without any significant change in spin population. The calculated vibrational modes associated with the N–N and N–O bonds correspond to 2375 and 1288 cm^{−1}, respectively, to be compared to the corresponding values, 2349 and 1326 cm^{−1}, respectively, for an isolated N₂O molecule. At the first transition state (Figure 4 and Table 6) we note a narrowing of the Fe–O bond length from 2.35 Å to 1.95 Å while the O–N bond length increases from 1.19 Å to 1.31 Å. After N₂ elimination and oxo-complex formation (configuration **III**), the Fe–Fe distance increases by 0.14 Å. The resulting Fe^I–O₍₁₎ bond distance of 1.63 Å is similar to that of a double bond and thus could be considered as a bond length of ferryl oxygen species. Moreover, the atomic spin densities on Fe^I decreases significantly from 3.59 in **II** to 3.21 in **III** which seems to correspond to the oxidation of Fe^{II} into Fe^{IV}. This interpretation goes in line with many experimental results attesting the existence of +4 oxidation state for iron ions.^{63–65} In a study devoted to a comparative analysis of Fe–oxygen complexes formed after reaction of N₂O or exposure to O₂, Jia et al.⁶³ reported that unsaturated Fe²⁺ ions react with N₂O to form ferryl groups where oxygen atoms are bound to Fe⁴⁺ ions. During the second adsorption–dissociation of N₂O molecule and upon going from **IV** to **V**, a spin density decrease of 0.57 of the highly coordinated Fe² is found. As for intermediate **III**, these results suggest a double Fe⁴⁺=O^{2−} bond character. The calculated vibrational modes associated with the Fe^I–O₍₁₎ and Fe²–O₍₂₎ stretching in $Z^-[\text{OFe}^1(\mu\text{-O})(\mu\text{-OH})\text{Fe}^2\text{O}]^+$ are respectively 847 cm^{−1} and 919 cm^{−1} which are close to a frequency values of a doubly bound adsorbed oxygen ($\nu_{\text{M=O}}$: 900–1100 cm^{−1}; M: metal).⁶⁶ Nevertheless, the natural population analysis evidence that the two oxo-groups in **V** are not equivalent (Table 5) which may result from the difference in the coordination number of the two iron cations. During the oxygen migration process (**V** → **VI**), the electronic population of the active site undergoes an interesting reorganization. On one hand there is a spin density transfer from the migrating oxygen species O₍₂₎ (see Table 5) to the neighboring iron atom (Fe² in configuration **VI** (Ms = 9)). The resulting mechanism can be attributed to the reduction of Fe^{IV} to Fe^{II}. On the other hand, a considerable spin density delocalization from the μ -peroxo and μ -hydroxo groups to the iron atom Fe^I induces a pronounced Fe^{IV}=O^{2−} character for Fe^I (spin density of

TABLE 5: Natural Charge and Natural Spin Population of Binuclear Iron Core of All Computed Local Minima of the N₂O Decomposition Path Illustrated in Figure 3^a

		Fe ^I	Fe ²	μ -O	μ -O _H	O _{NN}	O ₋₍₁₎	O ₋₍₂₎
conf I (Ms = 9)	charge	1.37	1.41	-1.20	-1.20	—	—	—
	spin	3.60	3.62	0.49	0.18	—	—	—
conf II (Ms = 9)	charge	1.41	1.41	-1.25	-1.21	-0.38	—	—
	spin	3.59	3.61	0.51	0.17	0.01	—	—
conf III (Ms = 9)	charge	1.57	1.47	-0.97	-1.15	—	-0.61	—
	spin	3.21	3.63	0.42	0.24	—	0.35	—
conf IV (Ms = 9)	charge	1.57	1.49	-1.00	-1.14	-0.38	-0.62	—
	spin	3.20	3.64	0.42	0.24	0.006	0.35	—
conf V (Ms = 9)	charge	1.60	1.55	-0.84	-1.05	—	-0.57	-0.51
	spin	3.25	3.07	0.38	0.33	—	0.29	0.54
conf VI (Ms = 9)	charge	1.47	1.45	-0.33	-1.17	—	-0.58	-0.59 ^b
	spin	3.06	3.60	0.07	0.2	—	0.75	0.13 ^b
conf VII (Ms = 9)	charge	1.70	1.47	-1.10	-1.17	—	-0.29	-0.29 ^b
	spin	3.92	3.66	0.70	0.22	—	-0.33	-0.33 ^b
conf VIII (Ms = 11)	charge	1.67	1.46	-1.10	-1.17	—	-0.29	-0.26 ^b
	spin	3.89	3.65	0.69	0.22	—	0.69	0.70 ^b

^a Fe^I and Fe² iron cations are coordinated to one (O_Z) and two (O_{Z1}, O_{Z2}) framework oxygen atoms, respectively. O_{NN}, O₋₍₁₎, and O₋₍₂₎ correspond to the adsorbed nitrous oxide O-end, first and second formed oxygen, respectively. ^b Migrated oxygen atom.

TABLE 6: Geometries and Imaginary Frequencies of the Calculated Transition States for N₂O Dissociation over the (μ -Oxo)(μ -hydroxo) Binuclear Ion Site

transition state	R_{N-N} (Å)	R_{N-O} (Å)	R_{Fe-O} (Å)	$\angle NNO$ (deg)	W (cm ⁻¹)
TS ₁	1.14	1.31	1.95	143.32	542.60 <i>i</i>
TS _{1a}	1.12	1.45	1.89	137.46	685.07 <i>i</i>
TS ₂	1.13	1.42	1.91	138.51	623.89 <i>i</i>
TS _{2a}	1.12	1.38	1.88	140.12	617.91 <i>i</i>

3.06). The calculated vibrational mode associated with the peroxo structure found at 875 cm⁻¹ falls within the O—O stretching frequency range observed in several metal peroxo model complexes ($\nu_{(O-O)} = 815-918$ cm⁻¹). After the recombination process, the superoxide structure is formed and is stable on the 11-et PES (configuration **VIII**). The analysis of spin density (3.89 for Fe^I and 3.65 for Fe²) suggests the formation of a mixed-valence Fe^{III}—Fe^{II} oxidation state. The O—O bond length of dioxygen in Z⁻[O₂Fe^I(μ -O)(μ -OH)Fe²]⁺ is calculated to be 1.32 Å on the two PESs. On the basis of the work of Che and Tench,⁶⁷ for an O—O bond length in the range 1.30–1.33 Å and a vibrational frequency in the range of 1015–1180 cm⁻¹, a superoxide O₂⁻ character is suggested. Similarly, the calculated dioxygen vibrational modes at 1177 and 1178 cm⁻¹ for the nonet and 11-et PES (**VIII**), respectively, suggest the formation, and therefore the desorption, of an O₂⁻ species.

N₂O decomposition energy profile investigations reveal that while the global reaction path is very comparable whatever the iron species, [Fe=O]⁺,^{17,24} [Fe—O—Fe]⁺,^{30,31} or [Fe(μ -O)(μ -OH)Fe]⁺, significant changes in energy barrier heights

are found. These results suggest that different rate-limiting steps are expected depending on the iron cation structures.

3.3. Antiferromagnetic Effects. Previous investigations^{30,31} on antiferromagnetic nature of binuclear iron complexes in Fe-ZSM-5 have demonstrated its small effect on the mechanistic aspects of the N₂O catalytic cycle such as the rate-limiting step and the approximate height of the reaction barriers. Cornell et al.⁶⁸ reported that the strength of antiferromagnetic coupling does not depend exclusively on the Fe—Fe distance but also on the angle Fe—X—Fe (X being a bridging group). The strongest magnetic couplings are suggested to occur for Fe—O—Fe bond angles between 120° and 180° and would decrease considerably for lower angle values. In the present work we evaluate the influence of a possible antiferromagnetic coupling between the two iron centers on a series of intermediates involved in the N₂O catalytic cycle. More precisely, we performed broken-symmetry calculations for the adsorption and dissociation steps of N₂O molecules over [Fe(μ -O)(μ -OH)Fe]⁺. As reported in Table 7, the magnitude of spin coupling constants J between the two iron centers is calculated to be very small for both minima and TS states. The energy difference between ferromagnetic and antiferromagnetic PES is 3.8 kcal/mol for the bare binuclear iron core (**I**) and 1.7 kcal/mol for the N₂O adsorbed state (**II**) and decreases to 0.2 kcal/mol for the oxo-complex (**III**). The effect of antiferromagnetic coupling on the activation energy is also found to be weak. The high energy barrier for the dissociation of the nitrogen molecule is calculated to be of 11.5 kcal/mol on the ferromagnetic PES and 11.1 kcal/mol on the antiferromagnetic PES. Therefore, as in the case of

TABLE 7: Relative Energies (calculated with reference to configurations **I), Fe—Fe Distances, and Fe—O—Fe and Fe—OH—Fe Bond Angles of Computed Configurations (**I**, **II**, TS₁, and **III**) on the Ferromagnetic and Antiferromagnetic PES^a**

	ferromagnetically coupled high spin states: Ms = 9				antiferromagnetically coupled broken symmetry states: Ms = 1				
	ΔE (kcal/mol)	Fe—Fe (Å)	$\angle FeXFe$ (deg)		ΔE (kcal/mol)	Fe—Fe (Å)	$\angle FeXFe$ (deg)		J (cm ⁻¹)
			X = O	X = OH			X = O	X = OH	
conf I	0.0	2.48	84.81	73.34	-3.8	2.51	87.26	74.45	-132.9
conf II	-7.0	2.53	86.18	75.22	-8.7	2.53	87.63	74.65	-59.4
TS ₁	4.5	2.59	89.12	78.88	2.4	2.59	91.00	78.07	-73.4
conf III	-34.8	2.63	91.93	80.31	-35.0	2.63	93.14	79.56	-7.0

^a Coupling constants calculated within the nonprojected approach (eq 7).

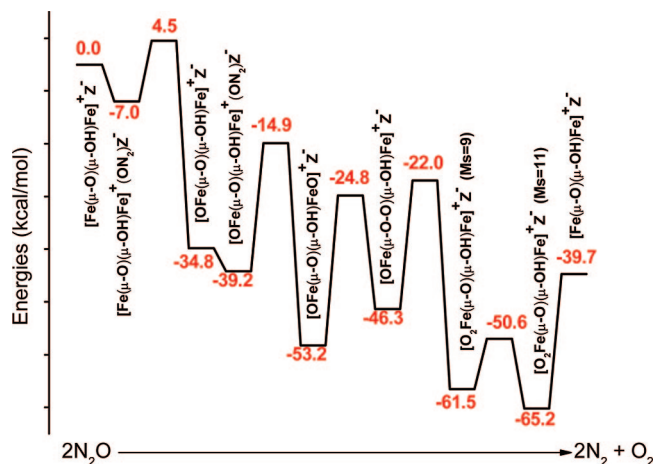


Figure 5. Reaction energy diagram of the nitrous oxide decomposition on dehydroxylated (μ -oxo)(μ -hydroxo) di-iron complex. All energies are zero-point corrected and are calculated with respect to the $Z^-[\text{Fe}(\mu\text{-O})(\mu\text{-OH})\text{Fe}]^+$ with appropriate amount of N_2O , N_2 , and O_2 . Energy values correspond to the ones reported in the reaction path.

TABLE 8: Free Energy Calculations [ΔG (T,P = 1 atm)] (in kcal/mol) for All Minima and Transitions States of the Computed N_2O Catalytic Reaction^a

	$\Delta G_{298\text{K}}$	$\Delta G_{400\text{K}}$	$\Delta G_{500\text{K}}$	$\Delta G_{600\text{K}}$	$\Delta G_{700\text{K}}$
conf I + $2\text{N}_2\text{O}_{(\text{g})}$	0.0	0.0	0.0	0.0	0.0
conf II + $\text{N}_2\text{O}_{(\text{g})}$	3.0	6.4	9.8	13.1	16.4
TS ₁ + $\text{N}_2\text{O}_{(\text{g})}$	14.7	14.8	18.3	21.8	25.3
conf III + $\text{N}_2\text{O}_{(\text{g})}$ + $\text{N}_{2(\text{g})}$	-33.7	-33.5	-33.4	-33.2	-33.1
conf IV + $\text{N}_{2(\text{g})}$	-27.8	-24.1	-20.6	-17.0	-13.5
TS ₂ + $\text{N}_{2(\text{g})}$	-2.8	1.3	5.2	9.1	13.0
conf V + $2\text{N}_{2(\text{g})}$	-50.9	-49.9	-49.4	-48.9	-48.4
TS ₃ + $2\text{N}_{2(\text{g})}$	-22.7	-22.4	-22.1	-21.8	-21.5
conf VI + $2\text{N}_{2(\text{g})}$	-43.4	-42.6	-41.8	-41.0	-40.3
TS _b + $2\text{N}_{2(\text{g})}$	-21.2	-21.3	-21.5	-21.5	-21.9
conf VII + $2\text{N}_{2(\text{g})}$	-60.0	-60.0	-60.0	-60.2	-60.3
MECP + $2\text{N}_{2(\text{g})}$	-50.6	-50.6	-50.6	-50.6	-50.6
conf VIII + $2\text{N}_{2(\text{g})}$	-63.8	-63.8	-63.9	-64.0	-64.2
conf I + O_2 + 2N_2	-48.6	-52.3	-55.9	-59.5	-63.0

^a Relative free energies are calculated with reference to configuration **I** with appropriate amounts of N_2O , N_2 , and O_2 .

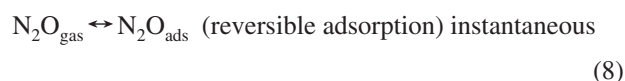
the $[\text{Fe}-\text{O}-\text{Fe}]^{2+}$ complex,^{30,31} antiferromagnetic coupling is expected not to influence significantly the reaction mechanism for $[\text{Fe}(\mu\text{-O})(\mu\text{-OH})\text{Fe}]^+$ complexes.

4. Analysis of the Computed Reaction Path and Comparison with Experimental Results

The calculated N_2O decomposition path on a (μ -oxo)(μ -hydroxo)-bridged binuclear iron core gives detailed information of the different elementary steps of the catalytic reaction. From experimental approaches, many recent mechanistic studies using transient techniques have identified the parameters for the elementary steps of N_2O decomposition and have developed a consistent kinetic model of the reaction.^{5,32,34,35,69} The overall investigated path calculated at 0 K (Figure 5) was considered to establish correlations between the present theoretical results and those reported over $[\text{Fe}-\text{O}-\text{Fe}]^{2+}$.³⁰ To get more insight in the kinetic behavior of our model, we analyzed the temperature effect on the investigated barrier heights by calculating the evolution of free energy values as a function of temperature for each elementary steps of the overall N_2O decomposition reaction (Table 8).

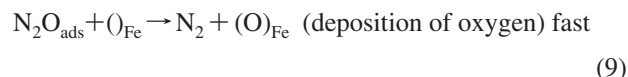
In the first step of the computed reaction model, N_2O is adsorbed over the Fe^{II} sites. This adsorption process is slightly

exothermic (Figure 5) and would correspond to the reversible adsorption of N_2O observed experimentally by Kiwi-Minsker et al.⁵ and introduced in their kinetic model by eq 8.

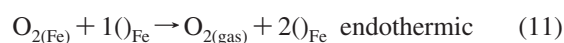


Therefore, one should note that the calculated ΔH_{ads} of -7.1 and -4.6 kcal/mol at 298 K for the adsorption of the first and second N_2O molecule, respectively, which are smaller than that measured experimentally (see section 3.2.1), are not surprising since DFT is known to not accurately reproduce weak bond interactions.⁷⁰ As a consequence, free energy calculations (Table 8) indicate an N_2O adsorption process that is entropically unfavorable. The calculated value of $T\Delta S$ ($T = 298$ K) of around 10 kcal/mol is relatively high and is understandable⁷¹ since it is dominated by transitional contributions to entropy of the bound linear N_2O .

To release molecular nitrogen via the dissociation of nitrous oxide-forming adsorbed oxygen species (eq 1), the reaction intermediates **II** and **IV** (Figure 3) should overcome a relatively small free energy barrier of 11.7 kcal/mol at 298 K for the first N_2O adsorbed molecule (eq 3) and a high free energy barrier of 25 kcal/mol for the second one (eq 5). This latter value increases up to 26.5 kcal/mol at $T = 700$ K. The oxygen formation processes are highly exothermic and lead to a highly stable intermediate in which each iron site is saturated by one oxygen atom. The surface atomic oxygen loading step was defined⁵ by eq 9:



The path for the desorption of molecular oxygen was calculated to occur after the migration of one deposited oxygen atom from one to the other iron site, followed by an O_2 recombination step (eq 10). The free energy barriers of 28.2 kcal/mol at 298 K and 26.9 kcal/mol at $T = 700$ K (Table 8) for the oxygen atom migration process are the highest barriers of the overall reaction mechanism. The oxygen atom migration process has therefore the slowest step (slower than the N_2O dissociation steps) of the whole computed reaction path. Oxygen recombination, which occurs by overcoming a relatively small free energy barrier of 17.5 kcal/mol at $T = 700$ K leads to highly stable intermediates containing different types of adsorbed molecular oxygen (with respect to the initial state, $\Delta G_{700\text{K}}$ (**VII**) = -60.3 kcal/mol and $\Delta G_{700\text{K}}$ (**VIII**) = -64.2 kcal/mol). Finally, the desorption reaction of molecular oxygen (eq 11) is calculated to be highly endothermic. Our results are consistent with many experimental findings which reveal that for lower temperatures the reaction pathways leading to molecular oxygen formation (eq 10) are slower than those leading to nitrogen formation.



Kondratenko et al.⁷² reported from transient experiments by TAP under vacuum conditions that while gaseous N_2 was observed from temperatures above 523 K, gaseous O_2 was only detected above 623 K. These authors explained this result by the fact that oxygen species originated upon N_2O decomposition are strongly bound to the catalyst surface.

These results are also consistent with transient-response experiments reported by Sun and co-workers,¹⁶ in which they observed for the high-temperature-treated catalyst that molecular oxygen desorption is slow compared to molecular nitrogen formation. These authors then concluded that the reaction rate over Fe-ZSM-5 is inhibited by molecular oxygen and they assigned this observation to a rate-limiting recombinative oxygen desorption.

In a recent paper of Kiwi-Minsker et al.⁵ the transient response curves of N₂O dissociation at temperature of 523 K revealed that no O₂ molecules are detected. The O₂ signal appeared only at temperatures higher than 623 K. Moreover, the steady-state kinetics at $T < 623$ K was found of zero order toward N₂O.³² This observation strongly suggests that at $T < 623$ K, upon N₂O adsorption and N₂ desorption, oxygen atoms are present on the surface, saturating iron active sites. This result strongly suggests the O₂ formation as the rate-limiting step of the overall catalytic cycle.

In contrast with these interpretations, Bell's group, on the basis of the calculated N₂O decomposition over Z[−][Fe=O]⁺ 17,24 and Z[−][Fe—O—Fe]²⁺Z[−] 30,31 sites, concluded that the N₂O dissociation is the rate-limiting step. These authors explained this finding by the observed first-order kinetic in N₂O partial pressure. Additionally, they concluded²⁴ that O₂ desorption cannot be a rate-limiting step, assuming that in such cases the catalyst surface would be saturated with oxygen species and N₂O decomposition would be zero order with respect to N₂O partial pressure.

It is important to note that most of the reported first-order kinetics of the N₂O decomposition on Fe-ZSM-5 were found at temperatures higher than 723 K. Under these conditions, the N₂O dissociation step consists of adsorption and dissociation processes that are entropically strongly unfavorable under most catalytic conditions (high temperature and small N₂O partial pressure). In contrast, the O₂ formation steps do not involve an entropically unfavorable step. These different behaviors are illustrated in Table 8. The evolutions of Δ*G* with increasing temperature show, on one hand, the slow decrease of the highest free energy barrier for O₂ formation process, and on the other hand, the increase of the highest free energy barrier for the second N₂O dissociation step. Otherwise, for kinetics applied at temperatures lower than 700 K, the step of atomic oxygen migration remains the largest barrier to overcome to achieve the N₂O decomposition cycle and therefore would be the rate-limiting step of the overall kinetics.

In conclusion, the temperature dependence of the activation free energies of the elementary steps 9 and 10 can explain the literature controversy on the observed kinetics order toward partial pressure of N₂O. The molecular oxygen formation is less sensitive to the temperature increase in comparison to the N₂ formation. As a consequence, while the highest free energy barrier corresponds to the O₂ formation below 700 K, it corresponds to the N₂ formation at temperatures above 700 K. The present results can explain the experimental switch of N₂O dissociation observed from a zero order at lower temperatures to a first-order kinetics at higher temperatures.⁵

5. Conclusion

The stability and the reactivity of the binuclear (μ-oxo)(μ-hydroxo)-bridged extra-framework iron cations in Fe-ZSM-5 has been investigated by DFT calculations. The results show that di-iron structure with geometric parameters close to EXAFS measurements is favorable. Geometric and spin population analysis of such a Z[−][Fe-(μ-O)(μ-OH)-Fe]⁺ precursor and

intermediates show that the two irons are not strictly equivalent. The calculated path for the N₂O decomposition shows for the first time that on such a di-iron complex, N₂O is readily adsorbed at low temperature and decomposes into N₂ and atomic oxygen adsorbed on each iron in a highly stable Z[−][O-Fe-(μ-O)(μ-OH)-Fe-O]⁺ intermediate. This process is followed by the atomic oxygen migration which occurs through the highest free energy barrier. This result suggests that the latter process is the rate-limiting step of the overall kinetics in agreement with many experimental results. The catalyst is regenerated after oxygen recombination and molecular oxygen desorption.

Acknowledgment. The authors thank Dr. Jeremy Harvey for advice concerning the use of his algorithm for MECP calculation. We gratefully acknowledge Pr. Dan Lerner and Dr. Ilaria Ciofi for helpful discussions. Computations were carried out on the IBM SP4 computers of the CINES (Centre Informatique National de l'Enseignement Supérieure) in Montpellier (France) and of the IDRIS (Institut des Ressources en Informatique Scientifique) in Orsay (France). The present work was financially supported by the European network of excellence IDE-CAT NMP-CT-2005-011730 WP.7.3 and by the convention 07CARN00301 of the Institut CARNOT "Chimie Environnementale et Développement Durable - Chimie Montpellier".

References and Notes

- Berthomieu, D.; Krishnamurty, S. *Quantum Chemical Calculations of Surfaces and Interfaces of Materials*; Basiuk, M. V. A., Ugliengo, P., Eds.; American Scientific Publishers: Valencia, CA, in press.
- Kapteijn, F.; Rodriguez-Mirasol, J.; Moulijn, J. A. *Appl. Catal. B* **1996**, *9*, 25.
- Wood, B. R.; Reimer, J. A.; Bell, A. T.; Janicke, M. T.; Ott, K. C. *J. Catal.* **2004**, *224*, 148.
- Wood, B. R.; Reimer, J. A.; Bell, A. T. *J. Catal.* **2002**, *209*, 151.
- Kiwi-Minsker, L.; Bulushev, D. A.; Renken, A. *Catal. Today* **2005**, *110*, 191.
- Zhu, Q.; Mojet, B. L.; Janssen, R. A. J.; Hensen, E. J. M.; Van Grondelle, J.; Magusin, P.; Van Santen, R. A. *Catal. Lett.* **2002**, *81*, 205.
- Perez-Ramirez, J.; Kapteijn, F.; Moulijn, J. A. *J. Catal.* **2002**, *208*, 211.
- Zecchina, A.; Rivallan, M.; Berlier, G.; Lamberti, C.; Ricchiardi, G. *Phys. Chem. Chem. Phys.* **2007**, *9*, 1.
- Panov, G. I.; Dubkov, K. A.; Starokon, E. V. *Catal. Today* **2006**, *117*, 148.
- Parmon, V. N.; Panov, G. I.; Uriarte, A.; Noskov, A. S. *Catal. Today* **2005**, *100*, 115.
- Pérez-Ramírez, J. *J. Catal.* **2004**, *227*, 512.
- Berlier, G.; Ricchiardi, G.; Bordiga, S.; Zecchina, A. *J. Catal.* **2005**, *229*, 127.
- Kapteijn, F.; Marbán, G.; Rodriguez-Mirasol, J.; Moulijn, J. A. *Catal.* **1997**, *167*, 256.
- Bulushev, D. A.; Kiwi-Minsker, L.; Renken, A. *J. Catal.* **2004**, *222*, 389.
- Sang, C.; Kim, B. H.; Lund, C. R. F. *J. Phys. Chem. B* **2005**, *109*, 2295.
- Sun, K.; Xia, H.; Hensen, E.; Van Santen, R.; Li, C. *J. Catal.* **2006**, *238*, 186.
- Heyden, A.; Peters, B.; Bell, A. T.; Keil, F. J. *Phys. Chem. B* **2005**, *109*, 1857.
- Delahay, G.; Bichon, P.; Capdeillacre, C. H.; Petitto, C. C. *Top. Catal.* **2008**, *6*, 19.
- Stirling, A. J. *Am. Chem. Soc.* **2002**, *124*, 4058.
- Martinez, A.; Goursot, A.; Coq, B.; Delahay, G. *J. Phys. Chem. B* **2004**, *108*, 8823.
- Yoshizawa, K.; Shiota, Y.; Yumura, T.; Yamabe, T. *J. Phys. Chem. B* **2000**, *104*, 734.
- Ryder, J. A.; Chakraborty, A. K.; Bell, A. T. *J. Phys. Chem. B* **2002**, *106*, 7059.
- Yakovlev, A. L.; Zhidomirov, M. G.; Van Santen, R. A. *J. Phys. Chem. B* **2001**, *105*, 12297.
- Heyden, A.; Bell, A. T.; Keil, F. J. *J. Catal.* **2005**, *233*, 26.
- Marturano, P.; Drozdova, L.; Kogelbauer, J. A.; Prins, R. *J. Catal.* **2000**, *192*, 236.
- Battiston, A. A.; Bitter, J. H.; Koningsberger, D. C. *Catal. Lett.* **2000**, *66*, 75.

- (27) Lazar, K.; Kotasthane, A. N.; Fejes, P. *Catal. Lett.* **1999**, *57*, 171.
- (28) Chen, H. Y.; El-Malki, E. M.; Wang, X.; Van Santen, R. A.; Sachtler, W. M. H. *J. Mol. Catal. A Chem.* **2000**, *162*, 159.
- (29) El-Malki, E. M.; van Santen, R. A.; Sachtler, W. M. H. *J. Phys. Chem. B* **1999**, *103*, 4611.
- (30) Hansen, N.; Heyden, A.; Bell, A. T.; Keil, F. J. *J. Phys. Chem. C* **2007**, *111*, 2092.
- (31) Hansen, N.; Heyden, A.; Bell, A. T.; Keil, F. J. *J. Catal.* **2007**, *248*, 213.
- (32) Kiwi-Minsker, L.; Bulushev, D. A.; Renken, A. *J. Catal.* **2003**, *219*, 273.
- (33) Kiwi-Minsker, L.; Bulushev, D. A.; Renken, A. *Catal. Today* **2004**, *91–92*, 165.
- (34) Pirngruber, G. D. *J. Catal.* **2003**, *219*, 456.
- (35) Mul, G.; Pérez-Ramírez, J.; Kapteijn, F.; Moulijn, J. A. *Catal. Lett.* **2001**, *77*, 7.
- (36) Panov, G. I.; Kharitonov, A. S.; Sobolev, V. I. *Appl. Catal.* **1993**, *98*, 1.
- (37) Panov, G. I. *CatTech* **2000**, *7*, 18.
- (38) Dubkov, K. A.; Ovanesyan, N. S.; Shteinman, A. A.; Starokon, E. V.; Panov, G. I. *J. Catal.* **2002**, *207*, 341.
- (39) Feng, X.; Hall, W. K. *Catal. Lett.* **1997**, *46*, 11.
- (40) Rice, M. J.; Chakraborty, A. K.; Bell, A. T. *J. Catal.* **1999**, *186*, 222.
- (41) Voskoboinikov, T. V.; Chen, H.-Y.; Sachtler, W. M. H. *Appl. Catal., B* **1998**, *19*, 279.
- (42) Guesmi, H.; Berthomieu, D.; Kiwi-Minsker, L. *Stud. Surf. Sci. Catal.* **2008**, *174*, 1123.
- (43) Parr, R. G.; Yang, W. *Density Functional Theory of Atoms and Molecules*; Oxford University Press: Oxford, U.K., 1989.
- (44) Becke, A. D. *Phys. Rev. A* **1988**, *37*, 785.
- (45) Lee, C.; Yang, W.; Parr, R. G. *Phys. Rev. B* **1988**, *37*, 785.
- (46) Schäfer, A.; Huber, C.; Ahlrichs, R. *J. Chem. Phys.* **1994**, *100*, 5829.
- (47) Kestner, N. R.; Combariza, J. E. In *Reviews in computational chemistry*; Lipkowitz, K. B., Boyd, D. B., Eds.; John Wiley and Sons: New York, 1999; Vol. 13, Chapter 2.
- (48) <http://www.gaussian.com/g03.htm> (2008).
- (49) http://www.Gaussian.com/g_whitepap/qst2 (2008).
- (50) http://www.Gaussian.com/g_whitepap/vib.html (2008).
- (51) Schröder, D.; Schwarz, H.; Shaik, S. *Metal-Oxo and Metal-Peroxo Species in Catalytic Oxidations*; Meunier, B., Ed.; Springer-Verlag: Berlin, 2000, pp 91–123.
- (52) Harvey, J. N.; Aschi, M.; Schwarz, H.; Koch, W. *Theor. Chem. Acc.* **1998**, *99*, 95, and references therein.
- (53) Harvey, J. N.; Aschi, M. *Phys. Chem. Chem. Phys.* **1999**, *1*, 5555.
- (54) Poli, R.; Harvey, J. N. *Chem. Soc. Rev.* **2003**, *32*, 1–8.
- (55) Ruiz, E.; Alvarez, S.; Carno, J.; Polo, V. *J. Chem. Phys.* **2005**, *123*, 164110.
- (56) *McQuarrie Statistical Mechanics*; Harper Collins Publishers Inc.: New York, 1976; p 56.
- (57) Chen, H. Y.; Sachtler, W. M. H. *Catal. Today* **1998**, *42*, 73.
- (58) Hall, W. K.; Feng, X.; Dumesic, J.; Watwe, R. *Catal. Lett.* **1998**, *52*, 13.
- (59) Wallar, B. J.; Lipscomb, J. D. *Chem. Rev.* **1996**, *96*, 2625.
- (60) Zheng, H.; Zhang, Y.; Dong, Y.; Young, V. G.; Que, L. *J. Am. Chem. Soc.* **1999**, *121*, 2226.
- (61) Zang, Y.; Pan, G.; Que, L.; Fox, B. G.; Münck, E. *J. Am. Chem. Soc.* **1994**, *116*, 3653.
- (62) Wood, B. R.; Reimer, J. A.; Bell, A. T. *J. Catal.* **2002**, *209*, 151.
- (63) Jia, J.; Sun, Q.; Wen, B.; Chen, L. X.; Sachtler, W. M. H. *Catal. Lett.* **2002**, *82*, 1.
- (64) Choi, S. H.; Wood, B. R.; Bell, A. T.; Janicke, M. T.; Ott, K. C. *J. Phys. Chem. B* **2004**, *108*, 8970.
- (65) Yuranov, I.; Bulushev, D. A.; Renken, A.; Kiwi-Minsker, L. *J. Catal.* **2004**, *227*, 138.
- (66) Tsyganenko, A. A.; Rodionova, T. A.; Filimonov, V. N. *React. Kinet. Catal. Lett.* **1979**, *11*, 113.
- (67) Che, M.; Tench, A. *J. Adv. Catal.* **1983**, *32*, 1.
- (68) Cornell, R. M. Schwertmann, U. *The Iron Oxides: Structure, Properties, Reactions Occurrence and Uses*; VCH: Weinheim, Germany, 1996.
- (69) Nobukawa, T.; Yoshida, M.; Okumura, K.; Tomishige, K.; Kuni-mori, K. *J. Catal.* **2005**, *229*, 374.
- (70) Bates, S. P.; Van Santen, R. A. *Adv. Catal.* **1998**, *42*, 1.
- (71) Watson, L. A.; Eisenstein, O. *J. Chem. Educ.* **2002**, *79*, 1269.
- (72) Kondratenko, E. V.; Rérez-Ramírez, J. *J. Phys. Chem. B* **2006**, *110*, 22586.

JP808044R